Photospheric properties and fundamental parameters of M dwarfs

A. S. Rajpurohit[1], F. Allard[2], G. D. C. Teixeira[3, 4], D. Homeier[5], S. Rajpurohit[6], O. Mousis[7]

[1] Astronomy & Astrophysics Division, Physical Research Laboratory, Ahmedabad 380009, India e-mail: `arvindr@prl.res.in`
[2] Univ Lyon, Ens de Lyon, Univ Lyon1, CNRS, Centre de Recherche Astrophysique de Lyon UMR5574, F-69007, Lyon, France
[3] Instituto de Astrofísica e Ciências do Espaço, Universidade do Porto, CAUP, Rua das Estrelas, 4150-762 Porto, Portugal
[4] Departamento de Física e Astronomia, Faculdade de Ciências, Universidade do Porto, Rua Campo Alegre, 4169-007 Porto, Portugal
[5] Zentrum für Astronomie der Universität Heidelberg, Landessternwarte, Königstuhl 12, 69117 Heidelberg, Germany
[6] Clausthal University of Technology, Institute for Theoretical Physics, Leibnizstr.10, 38678 Clausthal-Zellerfeld, Germany
[7] Aix Marseille Université, CNRS, LAM (Laboratoire d'Astrophysique de Marseille) UMR 7326, 13388, Marseille, France

ABSTRACT

Context. M dwarfs are an important source of information when studying and probing the lower end of the Hertzsprung-Russell (HR) diagram, down to the hydrogen-burning limit. Being the most numerous and oldest stars in the galaxy, they carry fundamental information on its chemical history. The presence of molecules in their atmospheres, along with various condensed species, complicates our understanding of their physical properties and thus makes the determination of their fundamental stellar parameters more challenging and difficult.

Aims. The aim of this study is to perform a detailed spectroscopic analysis of the high-resolution H-band spectra of M dwarfs in order to determine their fundamental stellar parameters and to validate atmospheric models. The present study will also help us to understand various processes, including dust formation and depletion of metals onto dust grains in M dwarf atmospheres. The high spectral resolution also provides a unique opportunity to constrain other chemical and physical processes that occur in a cool atmosphere.

Methods. The high-resolution APOGEE spectra of M dwarfs, covering the entire H-band, provide a unique opportunity to measure their fundamental parameters. We have performed a detailed spectral synthesis by comparing these high-resolution H-band spectra to that of the most recent BT-settl model and have obtained fundamental parameters such as effective temperature, surface gravity, and metallicity ($T_{\rm eff}$, $\log g$ and [Fe/H], respectively).

Results. We have determined $T_{\rm eff}$, $\log g$ and [Fe/H] for 45 M dwarfs using high-resolution H-band spectra. The derived $T_{\rm eff}$ for the sample ranges from 3100 to 3900 K, values of $\log g$ lie in the range $4.5 \le \log g \le 5.5$, and the resulting metallicities lie in the range $-0.5 \le$ [Fe/H] $\le +0.5$. We have explored systematic differences between effective temperature and metallicity calibrations with other studies using the same sample of M dwarfs. We have also shown that the stellar parameters determined using the BT-Settl model are more accurate and reliable compared to other comparative studies using alternative models.

Key words. Stars: low-mass – M dwarfs –Stellar atmosphere – fundamental parameters – atmospheres– late type

1. Introduction

The lower end of the Hertzsprung-Russell (HR) diagram has proven extremely useful in the last few decades as most of the very-low-mass stars (VLM) in the Galaxy are located in that region. Seventy percent of the Galactic stellar population (Bochanski et al. 2010) consists of these VLMs, in particular M dwarfs, and they contribute approximately 40% of the total stellar mass budget of the Galaxy (Gould et al. 1996; Mera et al. 1996; Henry 1998). Depending on its metallicity, the mass of any particular M dwarf ranges from 0.6 $M_\odot$ to the hydrogen-burning limit of about 0.075 $M_\odot$ (Chabrier et al. 2000). M dwarf populations show great diversity, in that one can find young metal-rich M dwarfs in open clusters, whereas galactic halos (Green & Margon 1994) and the globular clusters (Cool et al. 1996; Renzini et al. 1996) are known to host metal-poor M dwarfs that are billions of years old. Therefore, M dwarfs are one of the most important stellar components of the Galaxy, carrying fundamental information on the Galaxy's structure, formation, and chemical history. Recently, brown dwarfs and super earths were found around M dwarfs (Bonfils et al. 2012; Anglada-Escudé et al. 2016; Gillon et al.

2017) which makes them an important laboratory to study and understand their formation.

Despite the large number of M dwarfs in the Galaxy, a homogenous sample, in terms of age and metallicity, is very difficult to obtain, as high-resolution images and good S/N spectra are rare because of their intrinsics faintness. Moreover, the non-existence of true continuum makes it difficult or impossible to isolate different spectral diagnostics and to disentangle the effective temperature, surface gravity, and metallicity ($T_{\rm eff}$, $\log g$, and [Fe/H]). The presence of diatomic and triatomic molecules along with dust in M dwarf atmospheres, as we go from early to late M dwarfs, makes access to the spectral continuum nearly impossible both in the optical and in the near-infrared (NIR). Nevertheless, because of their cool temperature and low metal content, M dwarfs provide the best laboratory to study the dust and cloud formation as well as radiative transfer in their atmosphere.

As the $T_{\rm eff}$ of M dwarfs decreases from early to late M dwarfs, the optical and NIR spectra of M dwarfs indicate large numbers of diatomic (SiH, CaH, TiO, VO, CrH, FeH, OH, CO) and triatomic (CaOH, H_2O) molecules. The Rayleigh-Jeans branch of M dwarfs spectral energy distribution (SED) in Infra-

Red (IR) (>1.3 μm) is dominated by the H$_2$O and CO molecular absorption bands, whereas in the corresponding optical part (>0.4 μm) to near-IR (<1.3 μm) their SED is governed by TiO, VO and metal hydrides. Due to the presence of the these complex and crowded band structures, access to true continuum is not possible, and thus a pseudo-continuum is created, which usually shows the strongest and often resonant atomic lines at lower resolution (Allard 1990; Allard & Hauschildt 1995). In cooler M dwarfs with spectral type M6 or later, the outermost temperatures of their atmospheres are cool enough to form dust and clouds (see e.g., Tsuji et al. 1996b,a; Allard et al. 1997; Ruiz 1997; Allard et al. 1998). These various physical and chemical processes complicate the understanding of their cool atmospheres, thus making determination of their stellar properties even more difficult.

The proper classification of M dwarf spectra requires the comparison of a grid of synthetic spectra with observations. These comparisons can thus be used to derive M dwarfs' fundamental parameters. Such comparisons also help to disentangle and quantify basic physical properties and fundamental parameters such as T_{eff}, $\log g$, and [Fe/H]. Thus far, T_{eff}, $\log g$, and [Fe/H]) have not been determined for M dwarfs with great accuracy. Different groups have used various traditional techniques to estimate the T_{eff} of M dwarfs based on broadband photometry and black-body approximations. These relatively old, traditional techniques are not as reliable because the true continua of cool M-dwarfs is embedded in complex and broad molecular absorptions. Furthermore, in M dwarf atmospheres, the complexity increases significantly as dust and cloud formation occurs with decreasing T_{eff}. In the optical part of their SEDs, this can be seen as the weakening of TiO-, VO-, CaH-, and CaOH-band opacities by dust Rayleigh scattering, whereas as in the infrared (IR) region, the weakening of water bands occurs due to the greenhouse effect (Allard et al. 2001) or dust back-warming.

Models of the atmospheres of cool, low-mass stars and substellar objects have been the subject of tremendous development in recent decades (Brott & Hauschildt 2005; Helling et al. 2008; Allard et al. 2012, 2013). Because of this advancement, a number of studies is being carried out to derive the accurate stellar parameters of very-low-mass stars and brown dwarfs using both optical and near-infrared (NIR) observations (Burgasser & Kirkpatrick 2006; Bayo et al. 2014, 2017; Rajpurohit et al. 2012, 2013, 2014, 2016). Bayo et al. (2017) and Bayo et al. (2014) show the importance of consistent fundamental parameters by estimating their atmospheric parameters from optical and in the NIR with low-resolution spectra and photometry of M dwarfs, simultaneously. Through revised solar abundances by Asplund et al. (2009) and Caffau et al. (2011), and by incorporating updated atomic and molecular line opacities which govern the SED of M dwarfs, atmospheric models such as the BT-Settl (Allard et al. 2013) have seen major improvements in modeling various complex molecular absorption bands. These updated models now also include dust and cloud formation (Allard et al. 2013; Baraffe et al. 2015), which is important for cool M-dwarfs and metal-poor M subdwarfs (sdM), and thus yield promising results which explain the stellar-to-substellar transition and confirm the work of Rajpurohit et al. (2012).

In comparison to our Sun, the determination of atmospheric parameters for M dwarfs is very different and challenging. Stellar parameters, such T_{eff}, of M dwarfs remain model-dependent to some extent. There have been many attempts to derive the T_{eff} scale of M dwarfs with respect to constant age and metallicity. Due to the lack of very reliable model atmospheres in the past, Bessell (1991) used indirect methods to derive the T_{eff} scale of

M dwarfs based on black-body fitting to the NIR bands, whereas Wing & Rinsland (1979) and Veeder (1974) fitted much cooler black body to the optical. Tsuji et al. (1996b) and Casagrande et al. (2008) provided a good T_{eff} determination using an infrared flux method (IRFM) for dwarfs including M dwarfs. The M dwarfs in the Rayleigh Jeans tail (mostly red-wards of 2.5 μm) carry little flux compared to black body, thus the IRFM method tends to underestimate T_{eff} for M dwarfs. Boyajian et al. (2012) used another approach which is based on interferometrically determined radii and bolometric fluxes from photometry to calculate the T_{eff} for nearby K and M dwarfs, whereas Mann et al. (2015) determined the radius and mass by combining the empirical mass-luminosity relationships with evolutionary models, which in turn depend on the T_{eff} and metallicity.

Recently, Rajpurohit et al. (2013) determined the T_{eff} of nearby bright M dwarfs from the low-resolution spectra observed in the visible wavelength using the updated BT-Settl model atmosphere. Their study shows that these updated models can now reproduce the slope of their SED very well, unlike previous studies by Leggett et al. (1996, 1998, 2000, 2001) using previous versions of these models, which were using incomplete opacities and other inaccuracies. The $\log g$ of M dwarfs can be determined with the help of high-resolution spectra (Passegger et al. 2016; Rajpurohit et al. 2016). Passegger et al. (2016); Rajpurohit et al. (2016) used gravity-sensitive features such as Na I, K I and Ca I lines to determine the surface gravity in the optical. Other authors used interferometry to determine the angular diameter of the M dwarfs, together with mass-luminosity relations to derive the mass and $\log g$ (e.g. Ségransan et al. (2003)).

A proper metallicity calibration for M-dwarfs is essential to determine the planet star metallicity relation, which for FGK stars tends towards the super solar metallicities. The metallicity determination of M dwarfs can be done in two ways: photometric- and spectroscopic-based methods which are limited to the moderate-resolution spectra in the visible (Woolf & Wallerstein 2006; Woolf et al. 2009), and in the infrared (Mann et al. 2013a, 2014; Terrien et al. 2012; Rojas-Ayala et al. 2010; Newton et al. 2014). The former techniques use M dwarf photometry in the visible and infrared bands to create [Fe/H] calibrations (Bonfils et al. 2005; Johnson & Apps 2009; Schlaufman & Laughlin 2010), while the latter ones rely on low- to high-resolution spectra to measure indices and lines in order to establish spectroscopic calibrations or compare them to synthetic spectra, made from M dwarf atmospheric models (Valenti et al. 1998; Bean et al. 2006a,b; Lindgren & Heiter 2017). Recently Souto et al. (2017) presented the first detailed near-IR chemical abundance analysis observed by SDSS-IV-Apache Point Observatory Galactic Evolution Experiment (APOGEE, Majewski et al. (2015)). The T_{eff} values adopted in this study were derived from the photometric calibrations for M dwarfs by Mann et al. (2015) for the V-J and R-J colors.

In this paper, we take advantage of the updated BT-Settl model grid and high-resolution H-band spectra to determine the atmospheric parameters (T_{eff}, $\log g$ and [Fe/H]) of 45 M dwarfs. In Section 2, we briefly describe the observations and some aspects of data reduction. In Section 3, we describe the BT-Settl model atmosphere used in this study. Section 4 presents the results and describes the comparison with models and determination of stellar parameters. A Summary and Discussion are presented in Section 5.
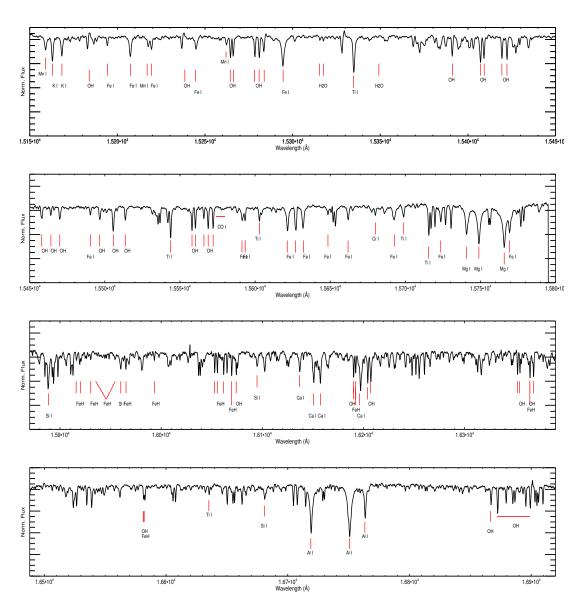
Fig. 1: APOGEE spectra of 2M11091225-0436249 (M0.5). The main spectral features can be seen, including atomic lines such as Fe I, Ca I, Na I, K I, Si I, Mg I, Al II, along with some hydride bands such as those of FeH and OH. We used mainly Souto et al. (2017) for the spectral feature recognition.

2. Observational data and sample selection

Regarding the details of the APOGEE survey along with data reduction the reader is referred to (Majewski et al. 2015; Wilson et al. 2010, 2012). The details of APOGEE M dwarfs ancillary project along with target selection and data reduction are described in Deshpande et al. (2013) and Nidever et al. (2015). We obtained spectra of 45 M dwarfs from Deshpande et al. (2013) M dwarfs ancillary project using SDSS-III Data release 12 (Alam et al. 2015). The spectral type and photometry are compiled using Simbad and Vizier catalog access through Centre de Donnees astronomiques de Strasbourg and are given in Table 1.

The presence of broad and complex molecular absorption in H-band makes this region one of the most difficult wavelength regimes for identifying various weak atomic absorption features in the spectra of M dwarfs. The dominant NIR features are due to photospheric absorption by H_2O, FeH, CO, OH, and neutral metals. The absorption lines of neutral metals, as well as the

bands of H_2O and CO, become stronger with decreasing T_{eff}. In the optical region, M dwarfs show strong features relative to the strength of the TiO and VO molecular bands. However, in the NIR regime, the dominant molecular features are due to H_2O. Also the single metal species such as FeH will not show the same level of decrease as the double metal TiO. The effect of collisional induced absorption (CIA) by H_2 on atomic spectral lines such as those of Fe I, Ca I, Na I, K I, Si I, Mg I, Al I, along with the strengthening of hydride bands such as those on FeH can be seen in their H-band spectra (Fig 1). As expected from the high log g of M dwarfs, the atomic features such as Ca I, Na I, and K I are massively pressure broadened. The OH and FeH produce more diffuse absorption NIR, unlike TiO and VO which produce distinctive band heads in the optical. The significant opacity source in the H band of M dwarfs is mainly FeH but its relative strength decreases and becomes saturated with decreasing temperature. In general one can see various prominent atomic lines such as Ca I, Na I, K I, Si I, Mg I, and Al I through-

Fig. 2: BT-Settl synthetic spectra from 4000 K to 3000 K at a step of 500 K (top to bottom in each panel) of H-band computed with PHOENIX radiative transfer code. The red and blue lines represent the synthetic spectra at [Fe/H] = +0.5 (red) and -0.5 (blue) for $T_{\rm eff}$ = 4000K , 3500K and 3000K at constant log g of 5.5.

out all the observed spectra. However, it is difficult to identify and measure the intensities of these atomic lines in the region where strong molecular absorption features are present.

The Ca I lines at 1.6136 μm, 1.6150 μm and 1.6157 μm, K I lines at 1.5163 μm and 156168 μm, Mg I lines at 1.5740 μm, 1.5748 μm, and 1.5765 μm, and Al I lines at 1.6718, 1.6750 and 1.6763 μm can bee seen in all the observed spectra. These atomic lines become broadened as one goes from early to later M dwarfs. As these atomic lines are so broad, their equivalent widths (EW) are of several angstroms. The strengths of these atomic features depend on various stellar parameters such as $T_{\rm eff}$, [Fe/H], and luminosity. These atomic lines which are relatively free from any blends, and which are not contaminated by telluric lines, are ideal features for studying their sensitivity to various stellar parameters.

3. Models and synthetic spectra

BT-Settl model atmosphere published by Allard et al. (2012, 2013) is used in this current study. Their computation of these models is performed with the PHOENIX radiative transfer code (Hauschildt et al. 1997; Allard et al. 2001) by assuming the hydrostatic and chemical equilibrium, convection using the mixing-length theory and a sampling treatment of the opacities. The grid of BT-Settl models extends from $T_{\rm eff}$ 300 to 7000 K in steps of 100 K, log g = 2.5 to 5.5 in steps of 0.5, and [M/H] = -2.5 to +0.5 in steps of 0.5 dex , accounting for alpha-enhancement and the latest solar abundances by Asplund et al.

(2009) and Caffau et al. (2011). The adopted [α/Fe] =-0.4 x [Fe/H] for -1 $\leq$ [Fe/H] $\leq$ 0 and [α/Fe] = +0.4 for all lower and +0.0 for supersolar metallicities, thus setting the "knee" of the alpha-enrichment relation to an average disk population value. These different α enhancements are mainly for the thin disc and thick disc (Edvardsson et al. 1993; Gratton et al. 1996; Fuhrmann 1998; Adibekyan et al. 2013). At a step of 0.1 dex in log g and metallicity we have interpolated the grid. The effect of metallicity and $T_{\rm eff}$ on various atomic and molecular features can bee seen in Figure 2 with varying $T_{\rm eff}$ from 4000 K (top) to 3000 K (bottom) with a step of 500 K and [Fe/H] = +0.5 (red) and -0.5 (blue) at constant log g of 5.0 in each panel. As found in previous studies (Leggett et al. 1998, 2000), log g has a relatively small influence on the SED of M dwarfs. But the significant effect of log g can been seen at high resolution on various atomic line profiles and also on various band systems, whereas metallicity has a large effect on the spectra. We have shown such effects in Figure 2 where one can see that with decreasing $T_{\rm eff}$, various atomic features start vanishing and molecular bands begin to dominate; in particular OH and FeH.

4. Results

4.1. Comparison with models and determination of stellar parameters

Spectral synthesis using synthetic spectra requires various parameters such as $T_{\rm eff}$, log g, and [Fe/H] and keeping the Sun as a reference. We followed the same procedure as used in Rajpuro-

Table 1: NIR photometry for our sample is taken from 2MASS along with their coordinates and spectral types.

2MASS ID 2MXXXXX	J	H	K_s	α	δ	SpT
00131578+6919372	08.55±0.024	07.98±0.02	07.74±0.02	03.315773	69.327003	M3.0
00321574+5429027	09.38±0.022	08.82±0.01	08.57±0.01	08.065590	54.4841	M4.5
00350487+5953079	11.03±0.022	10.40±0.02	10.16±0.02	08.77032	59.885548	M4.3
01195227+8409327	09.85 ±0.026	09.31±0.03	09.02±0.02	19.967825	84.159111	M5.0
02085359+4926565	08.42±0.023	07.81±0.01	07.58±0.02	32.223315	49.449055	M4.0
03152943+5751330	11.12±0.024	10.53±0.03	10.27±0.01	48.872662	57.85918	M3.5
03305473+7041145	09.48±0.018	08.93±0.01	08.67±0.01	52.728069	70.687378	M3.5
03425325+2326495	10.20±0.022	09.54±0.02	09.31±0.02	55.721897	23.447109	M4.0
04063732+7916012	10.03±0.027	09.48±0.02	09.19±0.02	61.655503	79.267006	M4.5
04125880+5236421	08.77±0.032	08.24±0.03	07.91 ±0.01	63.245023	52.611698	M4.0
05011802+2237015	10.16±0.020	09.59±0.02	09.23±0.01	75.325112	22.617104	M5.0
05030563+2122362	09.75±0.021	09.16±0.02	08.88±0.01	75.773472	21.376726	M5.0
05210188+3425119	11.87±0.021	11.31±0.01	11.02±0.01	80.257859	34.419991	M5.0
05470907-0512106	10.03±0.024	09.51±0.02	09.17±0.01	86.787800	-5.202969	M4.5
06115599+3325505	10.16±0.019	09.59±0.02	09.34±0.02	92.983296	33.430714	M3.5
06320207+3431132	10.69±0.021	10.14±0.01	09.86 ±0.01	98.008631	34.520336	M4.0
07140394+3702459	11.97±0.023	11.25 ±0.03	10.83±0.01	108.516439	37.046108	M8.0
08501918+1056436	11.28±0.023	10.67 ±0.02	10.40±0.02	132.579937	10.945469	M5.0
09301445+2630250	08.86±0.020	08.28 ±0.02	08.02±0.02	142.560229	26.506958	M3.0
10162955+0318375	10.85±0.023	10.26 ±0.02	10.00±0.02	154.123134	3.310419	M4.1
11005043+1204108	10.67±0.024	10.11±0.02	09.78±0.02	165.210134	12.069667	M5.0
11054316+1014093	08.64±0.021	08.04±0.05	07.79±0.02	166.429854	10.235927	M3.0
11091225-0436249	08.20±0.026	07.59 ±0.04	07.33±0.02	167.30107	-4.606939	M0.5
11474074+0015201	08.99±0.035	08.39± 0.04	08.09±0.02	176.919765	0.255604	M4.0
12045611+1728119	09.79±0.021	09.18 ± 0.02	08.96±0.02	181.233799	17.469975	M3.5
12232063+2529441	10.82±0.019	10.23 ±0.01	09.98±0.01	185.83597	25.495592	M3.7
12265737+2700536	10.19±0.024	09.60± 0.02	09.32±0.02	186.739043	27.014906	M4.5
13085059+1622039	09.26±0.022	08.65± 0.02	08.41±0.01	197.210793	16.36775	M3.0
13345147+3746195	09.71±0.02	09.14± 0.02	08.88±0.01	203.714472	37.772106	M3.5
13451104+2852012	09.88±0.022	09.31± 0.02	09.05±0.01	206.296026	28.867016	M3.4
14592508+3618321	10.25±0.018	09.64± 0.01	09.37±0.01	224.854502	36.308922	M3.5
16370146+3535456	11.13±0.022	10.54± 0.02	10.24±0.01	249.256085	35.596016	M6.0
18451027+0620158	07.65±0.019	07.04± 0.02	06.80±0.02	281.292808	6.337733	M1.0
18523373+4538317	10.49±0.020	09.93± 0.01	09.67±0.01	283.140551	45.642147	M5.0
18562628+4622532	09.59±0.021	09.01± 0.01	08.71±0.01	284.109528	46.381451	M4.0
19051739+4507161	09.85±0.021	09.30± 0.01	09.02±0.01	286.322483	45.121147	M4.0
19071270+4416070	10.44±0.020	09.85 ±0.01	09.55±0.01	286.802929	44.268635	M4.5
19081576+2635054	10.36±0.024	09.76±0.03	09.47±0.02	287.065699	26.584858	M5.0
19084251+2733453	09.75±0.026	09.23±0.03	08.95±0.01	287.177127	27.562593	M4.3
19321796+4747027	11.51±0.020	10.93±0.01	10.63 ±0.02	293.074865	47.78409	M5.0
19333940+3931372	08.12±0.020	07.56±0.02	07.33 ±0.01	293.414198	39.527016	M2.0
19430726+4518089	11.33±0.023	10.75±0.02	10.38±0.01	295.780281	45.302483	M5.5
19443810+4720294	11.81±0.021	11.28±0.01	11.00±0.01	296.158759	47.341515	M4.5
19510930+4628598	08.58±0.023	08.04±0.02	07.77±0.01	297.788774	46.483295	M4.0
21105881+4657325	09.87±0.022	09.26±0.01	09.05±0.01	317.745051	46.959034	M3.5

hit et al. (2014, 2016) to determine T_{eff}, $\log g$, and [Fe/H] using spectroscopic information in H-band. The typical $\log g$ of M dwarfs is approximately 5.0±0.2, except for the latest-type M dwarfs (Gizis 1997) and Casagrande et al. (2008); we therefore use models with $\log g$ = 4.5 - 5.5 for our analysis. To determine the stellar parameters of M dwarfs in our sample, we performed a χ^2 minimization using spectral synthesis employing the new BT-Settl model atmospheres across the entire wavelength range of the observed spectra. No weights are applied in our calcula-tion for different parameters. The synthetic spectral fitting is per-formed using the following steps: In the first step the synthetic spectra are convolved with an isotropic Gaussian profile with measured instrumental resolution which is then interpolated at each wavelength point of the observed spectra. In the following step we compared the observed spectra with that of the entire grid of models by taking the difference between the flux values of the observed and synthetic spectra at every wavelength point. Then, the sum of the squares of these differences is obtained for

Fig. 3: The effect of log g on the K I (top left), Mg I (top right), Ca I (bottom left) and Al I (bottom right) is clearly visible in BT-Settl synthetic spectra at $T_{\rm eff}$ = 3500 K and log g = 4.5 (black), 5.0 (blue), and 5.5 (red).

Fig. 4: APOGEE spectra of 2M11091225-0436249 (black) of spectral type M0.5 is compared with the best-fit BT-Settl (red). The best fit value for $T_{\rm eff}$, log g and [Fe/H] is 3900/4.5/-0.3.

each model in the grid, and the best model for each object is selected. We retain the best-match values of $T_{\rm eff}$, log g and [Fe/H] as first guess values on these three parameters. This step of syn-

thetic spectral fitting is performed on the set of models which have not been interpolated to a finer grid in log g and [Fe/H]. The comparison is made using a subsample of the model atmo-

Fig. 5: APOGEE spectra of 2M08501918+1056436 (black) of spectral type M5.0 is compared with the best-fit BT-Settl (red) synthetic spectra. The best fit $T_{\rm eff}$, $\log g$ and [Fe/H] is 3100/5.5/-0.0.

sphere grid covering the range of 3000 K $\leq T_{\rm eff} \leq$ 4000 K in steps of 100 K, -0.5 $\leq$ [Fe/H] $\leq$ 0.5 in steps of 0.5 dex, and 4.0 $\leq \log g \leq$ 5.5 in steps of 0.5 dex. During this step, we keep all the three parameters ($T_{\rm eff}$, $\log g$ and [Fe/H]) free. We excluded the spectral regions from 1.580 μm to 1.586 μm and from 1.642 μm to 1.649 μm because of the gap in blue to green and green to red arms of APOGEE.

In the second step, the parameters obtained for each object of our sample from the first step are used as an initial guess value and interpolation is done at a step of 0.1 dex in $\log g$ and [Fe/H]. Finally, every model of the grid covering the range of 3000 K $\leq T_{\rm eff} \leq$ 4000 K in steps of 100 K, -0.5 $\leq$ [Fe/H] $\leq$ 0.5 in steps of 0.1 dex, and 4.0 $\leq \log g \leq$ 5.5 in steps of 0.1 dex are again compar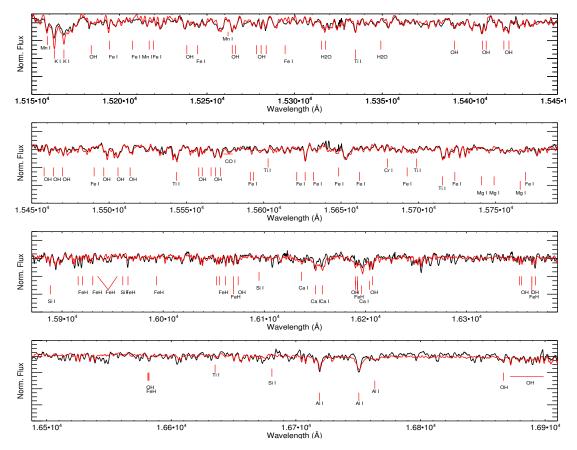ed to the observed spectrum at each wavelength point, and the χ^2 is calculated to determine the global minima. We retain models that give the lowest χ^2 values as the best fit parameters ($T_{\rm eff}$, $\log g$ and [Fe/H]) which are showed in Table 2. In the end, the best models are finally inspected visually by comparing them with the corresponding observed spectra. The uncertainties in Table 2 are based on standard deviation of the derived stellar parameters by accepting 1 σ variations from the minimum χ^2 which in all cases is calculated using constant χ^2 boundaries and is based on the χ^2 statistic.

We have also checked the behavior of synthetic spectra by visual inspection, looking at the shapes of various atomic species such as Fe I, Ca I, Na I, K I, Si I, Mg I, Al I and some molecular species such as OH, CO, and FeH (for details of the line list, see Souto et al. 2017). The OH-bands around 1.540 to 1.545 μm, 1.635 μm to 1.636 μm and 1.686 μm to 1.689 μm are insensitive

to variations of 0.5 dex in $\log g$ but are rather highly sensitive to $T_{\rm eff}$. However, at a given $\log g$ they shows huge variation over a change of only 100 K in $T_{\rm eff}$. We have conformed our $\log g$ by looking at the width of gravity-sensitive features such as the K I (1.5163 μm and 1.5168 μm), Ca I (1.6136 μm, 1.6150 μm, and 1.6157 μm), Al (1.6718 μm, 1.6750 μm, and 1.6763 μm), and Mg I (1.5740 μm, 1.5748 μm, and 1.5765 μm) along with the relative strength of metal hydride bands such as FeH. These features are particularly useful gravity discriminants for M dwarfs and sdM. The overall line strength increases with gravity because of high pressure mainly by H_2, He, and H I collisions and due to higher electron pressure on alkali lines (see Fig. 3). The effect of $\log g$ can be seen on width of the damping wings which, in addition, increases (Reiners 2005; Reiners et al. 2016). The effect of metallicity can also be seen on various atomic features where the molecular absorption is less and these atomic features appear clearly. The synthetic spectrum reproduces line profiles of various atomic lines such as Ti, Fe I, Ca I, Mg I, Si I, Mn I and Al I relatively well. The systematic errors are not eliminated, which arise due to missing or incomplete opacity sources (e.g., FeH-bands and OH and CO bands) are not eliminated (Baraffe et al. 2015) and the derived uncertainties are within the derived values of $T_{\rm eff}$, $\log g$, and [Fe/H]
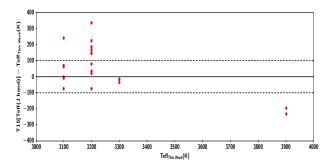
5. Summary and Discussion

The high-resolution spectra with good signal-to-noise ratio of M dwarfs is very important and necessary to determine the $T_{\rm eff}$, $\log g$, and [Fe/H], and also the individual element abundances to
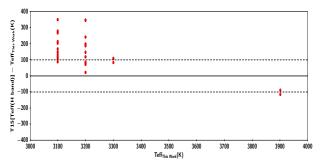
Table 2: Stellar parameters of the observed targets determined by minimizing χ^2. The uncertainty in T_{eff} (K) is ± 100 K, whereas for log g (cm s^{-2}) and [Fe/H] is given below.

2MASS ID 2MASS J	This study T_{eff}/ log g /[Fe/H]	Terrien et al. (2015) T_{eff}, [Fe/H] using Mann et al. (2013b) J, H and K calibration	Terrien et al. (2015) T_{eff}, [Fe/H] using Newton et al. (2014) calibration
00131578+6919372	3200 / 5.5±0.3 / -0.3±0.04	–	–
00321574+5429027	3200 / 5.5±0.3 / -0.2±0.04	3366/3271/3285, -0.03/-0.08/-0.05	3206/+0.00
00350487+5953079	3100 / 5.5±0.3 / -0.0±0.05	–	–
01195227+8409327	3100 / 5.5±0.3 / -0.3±0.06	–	–
02085359+4926565	3200 / 5.5±0.3 / -0.1±0.05	3280/3285/3330, +0.08/+0.03/+0.05	3347/+0.14
03152943+5751330	3200 / 5.5±0.3 / -0.3±0.05	–	–
3305473+7041145	3200 / 5.5±0.3 / -0.3±0.05	–	–
03425325+2326495	3200 / 5.5±0.3 / -0.0±0.05	–	–
4063732+7916012	3100 / 5.5±0.2 / -0.0±0.06	–	–
04125880+5236421	3100 / 5.5±0.3 / -0.0±0.05	3026/3304/3276, +0.02/-0.08/-0.02	–/+0.06
05011802+2237015	3200 / 5.5±0.5 / -0.5±0.04	–/3223/3277, +0.21/+0.03/+0.12	–/+0.20
05030563+2122362	3100 / 5.5±0.2 / -0.1±0.07	–/3223/3277, +0.13/+0.02/+0.02	–/+0.05
05210188+3425119	3100 / 5.5±0.3 / -0.5±0.04	–	–
05470907-0512106	3100 / 5.5±0.3 / -0.3±0.06	–	–
06115599+3325505	3100 / 5.5±0.2 / -0.1±0.07	3099/3207/3276, +0.02/+0.12/+0.01	–/+0.13
06320207+3431132	3200 / 5.5±0.3 / -0.4±0.05	3126/3388/3313, -0.03/-0.05/-0.09	–/+0.03
07140394+3702459	3000 / 5.5±0.2 / -0.5±0.11	–	–
08501918+1056436	3100 / 5.5±0.2 / -0.0±0.06	–	–
09301445+2630250	3300 / 5.0±0.5 / -0.3±0.05	3285/3384/3359, +0.04/+0.13/+0.13	3410/+0.21
10162955+0318375	3200 / 5.5±0.3 / -0.2±0.03	3345/3399/3328, -0.03/+0.03/-0.05	3217/+0.00
11005043+1204108	3100 / 5.5±0.2 / -0.5±0.11	–/3304/3276, +0.12/-0.07/-0.11	–/+0.05
11054316+1014093	3200 / 5.0±0.5 / -0.0±0.05	3422/3547/3418, -0.08/-0.10/-0.05	3357/+0.01
11091225-0436249	3900 / 4.5±0.5 / -0.3±0.04	3670/3786/3803, -0.04/-0.14/-0.04	3659/-0.07
11474074+0015201	3200 / 5.5±0.3 / -0.4±0.04	–/3320/3300, +0.10/+0.1/5 +0.03	–/+0.17
12045611+1728119	3200 / 5.5±0.2 / -0.1±0.07	3235/3318/3330, -0.09/-0.11/-0.03	3303/+0.05
12232063+2529441	3300 / 5.0±0.5 / -0.4±0.04	3267/3409/3344, -0.05/-0.01/+0.05	3303/+0.05
12265737+2700536	3100 / 5.5±0.3 / -0.0±0.06	–/3304/3280, +0.13/-0.05/ +0.02	–/+0.11
13085059+1622039	3200 / 5.5±0.4 / -0.4±0.04	3533/3545/3407, -0.15/-0.10/-0.15	–/+0.11
13345147+3746195	3200 / 5.5±0.3 / -0.1±0.04	3219/3348/3297, +0.13/-0.01/+0.14	–/+0.22
13451104+2852012	3200 / 5.0±0.5 / -0.4±0.04	3385/3441/3383, -0.09/-0.16/-0.09	3399/-0.11
14592508+3618321	3200 / 5.5±0.3 / -0.0±0.04	–	–
16370146+3535456	3100 / 5.5±0.2 / -0.5±0.04	–	–
18451027+0620158	3900 / 4.5±0.5 / -0.4±0.04	3707/3812/3779, +0.03/+0.07/-0.03	3664/-0.05
18523373+4538317	3100 / 5.5±0.2 / -0.0±0.07	3169/3219/3285, -0.00/-0.08/-0.06	–/-0.03
18562628+4622532	3100 / 5.5±0.3 / -0.0±0.05	3091/3379/3307, +0.06/-0.14/-0.03	–/+0.05
19051739+4507161	3100 / 5.5±0.3 / -0.2±0.04	3339/3314/3313, -0.06/-0.23/-0.17	3215/-0.14
19071270+4416070	3100 / 5.5±0.3 / -0.3±0.06	3163/3269/3288, +0.2/2-0.0/2+0.19	–/+0.25
9081576+2635054	3100 / 5.5±0.3 / -0.4±0.06	4747/3449/3280, +0.77/+0.10/+0.26	–/+0.29
19084251+2733453	3100 / 5.5±0.3 / -0.2±0.04	–/3368/3316,+0.42/-0.28/-0.30	3217/-0.32
19321796+4747027	3100 / 5.5±0.3 / -0.3±0.05	–	
19333940+3931372	3200 / 5.5±0.3 / -0.1±0.05	–	
19430726+4518089	3100 / 5.5±0.2 / -0.5±0.06	–	
19443810+4720294	3100 / 5.5±0.3 / -0.5±0.04	–	
19510930+4628598	3200 / 5.5±0.3 / -0.0±0.07	–/3279/3295, +0.06/-0.09/-0.07	–/+0.07
21105881+4657325	3300 / 5.0±0.5 / -0.2±0.06	–	

a high accuracy. This paper presents the results from the spectral synthesis analysis to determine the fundamental parameters form the high-resolution APOGEE H-band spectra for early to mid M dwarfs using the updated BT-Settl model. In the NIR, particularly in H band, the BT-Settl model has never been tested before with the high-resolution spectra of M dwarfs. Therefore, our present study constitutes a benchmark for model atmospheres of low-mass stars in NIR. The physical parameters T_{eff}, log g, and [Fe/H] for stars of our sample is determined by comparing the observed spectra with the synthetic spectra. The main purpose of this paper is to disentangle the parameter space (T_{eff}, log g, and [Fe/H]) with independent information on atmospheric parameters. The comparison of observed spectra with the synthetic spectra is crucial to reveal the inaccuracy or incompleteness of
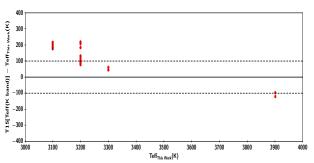
Fig. 6: Difference between the T_{eff} calibrations from Terrien et al. (2015, T15), estimated for the M dwarfs from Mann et al. (2013b) J (top), H (middle) and K_s (bottom) calibrations and T_{eff} from this work. On the horizontal axis we show the T_{eff} that we infer from our best fit BT-Settl model used in this work. The black full line represents the origin and the dashed black lines represent the error from the grid size of 100K.

Fig. 7: Difference between the T_{eff} calibrations from Terrien et al. (2015, T15) , estimated for the M dwarfs from H-band relationships given by Newton et al. (2015), calibrations, and T_{eff} from this work. On the horizontal axis we show the T_{eff} that we infer from our best fit BT-Settl model used in this work. The black full line represents the origin and the dashed black lines represent the error from the grid size of 100K.
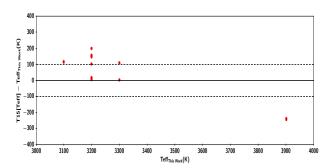
the opacities used in the model. The atmospheric parameters derived from the comparison between our sample and the BT-Settl

model are summarized in Table 2. For example, Figs. 4 and 5 show the comparison of the best-fit BT-Settl model (red) with the star of spectral type M1.0 and M3.0 (black) in our sample. Their best fit parameters are given in Table 2. The specific strengths of the CO, OH, and FeH-band heads are very well reproduced by the synthetic spectra over the entire M dwarf sequence, showing that the nosy pattern visible at this high spectral resolution is not noise.

The BT-Settl models also predict and reproduce the shape of various atomic lines such as Ca I, Na I, K I, Si I, Mg I, Al I, Ti I rather well and their strengths are well fitted. The observed atomic lines in the spectra are broader and shallower than those predicted by the BT-Settl model in the cooler M dwarfs (spectral type M3 or later). The qualitative behavior of the K I, Al I, Mg I, Ti I and Ca I lines is well reproduced by the BT Settl model as compared to the strong pressure-broadening wings in the early to mid M dwarfs. In the early M dwarfs, the cores of the observed K I, Al I, Mg I and Ca I lines are still visible. The broader absorption component of the atomic lines becomes saturated in M dwarfs later than M6 which were extending a few tens to one hundred angstroms.

The T_{eff} is the parameter that causes the largest uncertainty while determining the other stellar parameters of M dwarfs; their metallicity in particular. Our results for T_{eff} are in good agreement with the T_{eff} as a function of spectral type given in Rajpurohit et al. (2013). Now we compare our T_{eff}, $\log g$, and [Fe/H] determination to other works such as Terrien et al. (2015); Schmidt et al. (2016). Terrien et al. (2015) measured the T_{eff} for the M dwarfs using color–T_{eff} relations with the method described by Mann et al. (2013b) along with different temperature indices such as H_2O-K2 (Rojas-Ayala et al. 2012), H_2O-H Terrien et al. (2012) and Mann et al. (2013a). Figure 6 shows the comparison of our measured T_{eff} with Terrien et al. (2015) which clearly shows that Terrien et al. (2015) overestimates in lower T_{eff} and underestimates in higher T_{eff} among the various calibrations using J, H and K_s bands, when compared to our T_{eff} determinations. This discrepancy could be due to that fact that their determination was based on near-infrared spectra using the SpeX spectrograph which has significantly lower resolution, and many of their individual determinations were from the J/H/K bands which give relatively inconsistent results. These empirical relations give smaller errors as compared to NIR but they are not as precise as model-fitting techniques. We have also compared the T_{eff} calculated by Terrien et al. (2015) based on H-band atomic feature strengths such as Al I, Mg I, K I, Si I (Fig 7) using the strength of atomic features studied in Newton et al. (2015). We find an offset of around 200 K between our T_{eff} and Terrien et al. (2015) which could be due to the fact that Newton et al. (2015) used a limited number of atomic lines for equivalent width in their analysis where the accurate continuum placement could be the issue.

In four of the stars common common to both ours and the Schmidt et al. (2016) sample, we find that for stars 2MASSJ 11091225-0436249 and 2MASSJ 18451027+0620158, the T_{eff} by Schmidt et al. (2016) is 200 to 300K lower than our measurements, whereas for 2MASSJ 19333940+3931372 and 2MASSJ 21105881+4657325 the T_{eff} by Schmidt et al. (2016) is 200 to 300K higher. Schmidt et al. (2016) determine the T_{eff}, $\log g$, and [Fe/H] of late-K and early-M dwarfs selected from the APOGEE spectroscopic survey using ASPCAP (APOGEE Stellar Parameters and Chemical Abundances Pipeline) (García Pérez et al. 2016). ASPCAP uses APOGEE ATLAS9 models (Mészáros et al. 2012). For this same set of four targets, we have compared $\log g$ and [Fe/H] with Schmidt et al. (2016) and found
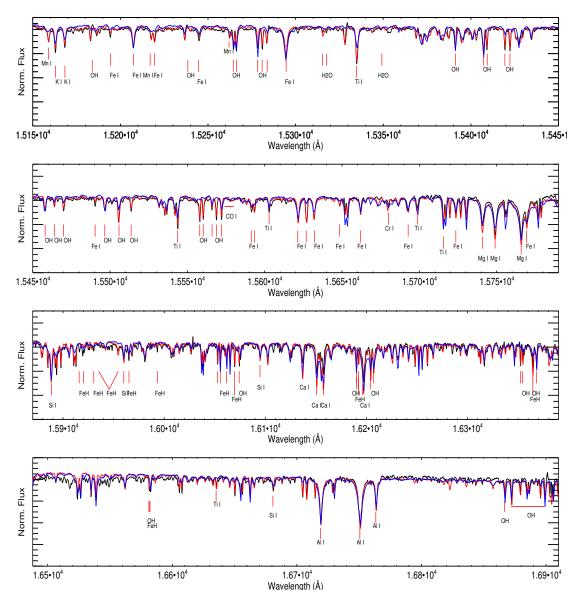
Fig. 8: APOGEE spectra of 2M11091225-0436249 (black) of spectral type M0.5 is compared with the best-fit BT-Settl (red) and MARCS model (blue). The best fit value for T_{eff}, log g and [Fe/H] is 3900/4.5/-0.3.

a systematic offset of around 0.5 dex to 1.0 dex. We have also compared the best-fit BT-Settl model (red) and MARCS model (blue) with observed spectra of 2M11091225-0436249 and 2M08501918+1056436 (back). We have chosen the identical atmospheric parameters for MARCS model as mentioned in Table 2. We obtain the MARCS (Gustafsson et al. 2008) model which was calculated in 2012 and distributed on the MARCS website[1]. It is clear from Figs. 8 and 9 that in the MARCS model, many OH, CO, and FeH bands are missing. Also, the line strength of various atomic species, such as K I, Ti I, Ca I and Al I, is weaker in the MARCS model than in the BT-Settl model which could be due to low-resolution flux samples as provided on the MARCS website. This discrepancy may also be due to the use of somewhat different assumptions concerning convection, and input data such as continuous opacities in MARCS and ATLAS9 models as compared to the BT-Settl model. Exploring such effects is beyond the scope of this study but a proper way

would be to compare the best fit parameters derived using different sets of models, which would provide information on model systematics. For the BT-Settl model, a crucial test is to check its consistent accuracy.

Metallicity is a parameter which cannot be constrained independently, but can be determined from spectroscopic analysis. We have also compared our [Fe/H] determination with spectroscopically determined metallicity estimates from Terrien et al. (2015) (see Figs. 10 and 11). Terrien et al. (2015) used both J, H, and K_s band calibration given by Mann et al. (2013b) and the combinations of EW that effectively trace stellar metallicity from the H-band spectra given by Newton et al. (2014). Terrien et al. (2015) estimated the metallicities of the M dwarfs using the EW of the NaI feature at 2.2 μm in the K band of Infrared Telescope Facility (IRTF) spectra as used by Newton et al. (2014). We find an average deviation of 0.2 to 0.4 dex in [Fe/H] from Newton et al. (2014) and Terrien et al. (2015). A possible explanation for this deviation could problems or differences in the determination of T_{eff}. The [Fe/H] and T_{eff} are dependent to the point
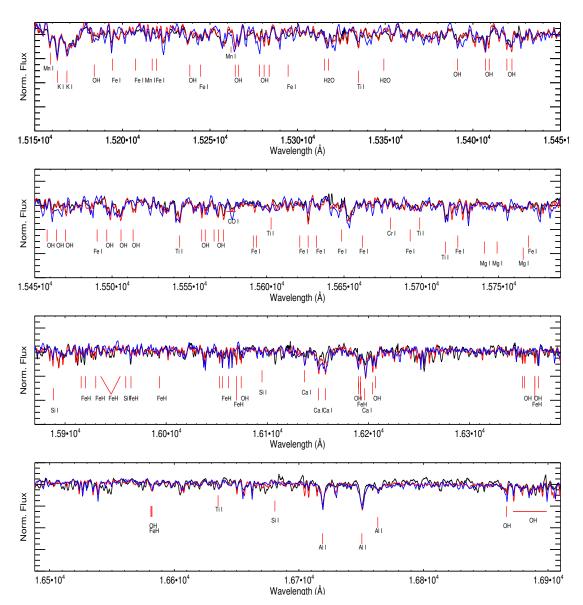
---

[1]http://marcs.astro.uu.se

Fig. 9: APOGEE spectra of 2M08501918+1056436 (black) of spectral type M5.0 is compared with the best-fit BT-Settl (red) and MARCS model (blue). The best fit value for T_{eff}, $\log g$ and [Fe/H] is 3100/5.5/-0.0.

where there is normally a degeneracy of models based on this interdependence. The different parameter combinations of T_{eff} and $\log g$ can produce the same [Fe/H] at low resolution. These deviations could also be due to the fact that the BT-Settl model provides a better description of the M dwarf atmospheres and therefore more accurate metallicities can be derived than when using other methods, which is also pointed out by Lindgren & Heiter (2017).

The recent improvement in the BT-Settl model atmosphere could have implications beyond those noted in this study. The description of various physical process at these low temperatures is well explained by BT-Settl models. These models now provide a better fit to the high-resolution spectroscopic observations of M dwarfs and help in accurately determining their atmospheric parameters. To address our offset in metallicity using different sets of model atmospheres, we also made a comparison study with the MARCS model. This comparison suggests that the BT-Settl models describe cool atmospheres more accurately than the MARCS model. We plan to use our method along

with the grid of these new BT-Settl models to estimate the stellar parameter of M dwarfs both in optical and in NIR spectra and photometry simultaneously to minimize the differences. The improvements in BT-Settl (Allard et al. 2013), achieved with the revision of solar abundances by Asplund et al. (2009) and Caffau et al. (2011), and by including updated atomic and molecular line opacities that dominate both in the optical and NIR range M dwarfs, greatly help to reproduce the extensive and complex molecular absorption band systems present in M dwarf atmospheres.

As compared to other models, the line strength and shape of various atomic and molecular features is very well reproduced by the BT-Settl models but there is still need for improvement in the regions where the fit is not good. This could be due to the lack of various opacity line lists in the model; in particular the FeH line list is missing in the H bandpass. Currently, the ExoMol group is developing an accurate and complete line list for TiO which is the next step to including them in the BT-Settl model before computing detailed model atmosphere grids and interior
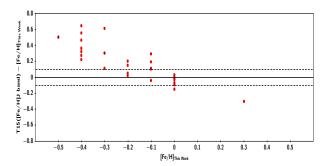
Fig. 10: Difference between the [Fe/H] calibrations from Terrien et al. (2015, T15), estimated for the M dwarfs from H-band relationships given by Newton et al. (2014) calibrations and [Fe/H] from this work. On the horizontal axis we show the [Fe/H] that we infer from our best fit BT-Settl model used in this work. The black full line represents the origin and the dashed black lines represent the error from the grid size of 0.1 dex.
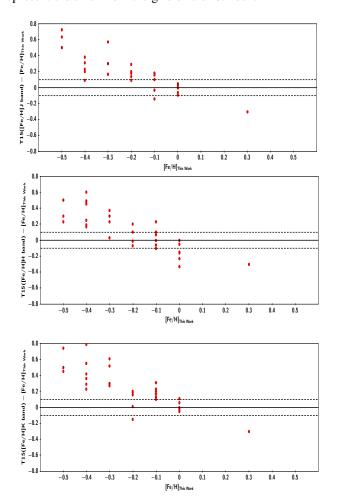

Fig. 11: Difference between the [Fe/H] calibrations from Terrien et al. (2015, T15), estimated for the M dwarfs from Mann et al. (2013b) J (top), H (middle) and K_s (bottom) calibrations and [Fe/H] from this work. On the horizontal axis we show the [Fe/H] that we infer from our best fit BT-Settl model used in this work. The black full line represents the origin and the dashed black lines represent the error from the grid size of 0.1 dex.

and evolution models at finer steps in the atmospheric parameters. The three-dimensional radiative hydrodynamics simulations and radiative transfer will help in understanding the effects

of temperature inhomogeneities in the atmosphere which begin to have greater impact on the spectrum formation.

References

Adibekyan, V. Z., Figueira, P., Santos, N. C., et al. 2013, A&A, 554, A44
Alam, S., Albareti, F. D., Allende Prieto, C., et al. 2015, ApJS, 219, 12
Allard, F. 1990, PhD thesis, PhD thesis. Ruprecht Karls Univ. Heidelberg, (1990)
Allard, F., Alexander, D. R., & Hauschildt, P. H. 1998, in Astronomical Society of the Pacific Conference Series, Vol. 154, Cool Stars, Stellar Systems, and the Sun, ed. R. A. Donahue & J. A. Bookbinder, 63–+
Allard, F. & Hauschildt, P. H. 1995, ApJ, 445, 433
Allard, F., Hauschildt, P. H., Alexander, D. R., & Starrfield, S. 1997, ARA&A, 35, 137
Allard, F., Hauschildt, P. H., Alexander, D. R., Tamanai, A., & Schweitzer, A. 2001, ApJ, 556, 357
Allard, F., Homeier, D., & Freytag, B. 2012, Royal Society of London Philosophical Transactions Series A, 370, 2765
Allard, F., Homeier, D., Freytag, B., et al. 2013, Memorie della Societa Astronomica Italiana Supplementi, 24, 128
Anglada-Escudé, G., Amado, P. J., Barnes, J., et al. 2016, Nature, 536, 437
Asplund, M., Grevesse, N., Sauval, A. J., & Scott, P. 2009, ARA&A, 47, 481
Baraffe, I., Homeier, D., Allard, F., & Chabrier, G. 2015, A&A, 577, A42
Bayo, A., Barrado, D., Allard, F., et al. 2017, MNRAS, 465, 760
Bayo, A., Rodrigo, C., Barrado, D., & Allard, F. 2014, Mem. Soc. Astron. Italiana, 85, 773
Bean, J. L., Benedict, G. F., & Endl, M. 2006a, ApJ, 653, L65
Bean, J. L., Sneden, C., Hauschildt, P. H., Johns-Krull, C. M., & Benedict, G. F. 2006b, ApJ, 652, 1604
Bessell, M. S. 1991, AJ, 101, 662
Bochanski, J. J., Hawley, S. L., Covey, K. R., et al. 2010, AJ, 139, 2679
Bonfils, X., Forveille, T., Delfosse, X., et al. 2005, A&A, 443, L15
Bonfils, X., Gillon, M., Udry, S., et al. 2012, ArXiv e-prints
Boyajian, T. S., von Braun, K., van Belle, G., et al. 2012, ApJ, 757, 112
Brott, I. & Hauschildt, P. H. 2005, in ESA Special Publication, Vol. 576, The Three-Dimensional Universe with Gaia, ed. C. Turon, K. S. O'Flaherty, & M. A. C. Perryman, 565
Burgasser, A. J. & Kirkpatrick, J. D. 2006, ApJ, 645, 1485
Caffau, E., Ludwig, H.-G., Steffen, M., Freytag, B., & Bonifacio, P. 2011, Sol. Phys., 268, 255

Casagrande, L., Flynn, C., & Bessell, M. 2008, MNRAS, 389, 585
Chabrier, G., Baraffe, I., Allard, F., & Hauschildt, P. 2000, ApJ, 542, 464
Cool, A. M., Piotto, G., & King, I. R. 1996, ApJ, 468, 655
Deshpande, R., Blake, C. H., Bender, C. F., et al. 2013, AJ, 146, 156
Edvardsson, B., Andersen, J., Gustafsson, B., et al. 1993, A&A, 275, 101
Fuhrmann, K. 1998, A&A, 338, 161
García Pérez, A. E., Allende Prieto, C., Holtzman, J. A., et al. 2016, AJ, 151, 144
Gillon, M., Triaud, A. H. M. J., Demory, B.-O., et al. 2017, ArXiv e-prints
Gizis, J. E. 1997, AJ, 113, 806
Gould, A., Bahcall, J. N., & Flynn, C. 1996, ApJ, 465, 759
Gratton, R. G., Carretta, E., & Castelli, F. 1996, A&A, 314, 191
Green, P. J. & Margon, B. 1994, ApJ, 423, 723
Gustafsson, B., Edvardsson, B., Eriksson, K., et al. 2008, A&A, 486, 951
Hauschildt, P. H., Baron, E., & Allard, F. 1997, ApJ, 483, 390
Helling, C., Ackerman, A., Allard, F., et al. 2008, MNRAS, 391, 1854
Henry, T. J. 1998, in Astronomical Society of the Pacific Conference Series, Vol. 134, Brown Dwarfs and Extrasolar Planets, ed. R. Rebolo, E. L. Martin, & M. R. Zapatero Osorio, 28–+
Johnson, J. A. & Apps, K. 2009, ApJ, 699, 933
Leggett, S. K., Allard, F., Berriman, G., Dahn, C. C., & Hauschildt, P. H. 1996, ApJS, 104, 117
Leggett, S. K., Allard, F., Dahn, C., et al. 2000, ApJ, 535, 965
Leggett, S. K., Allard, F., Geballe, T. R., Hauschildt, P. H., & Schweitzer, A. 2001, ApJ, 548, 908
Leggett, S. K., Allard, F., & Hauschildt, P. H. 1998, ApJ, 509, 836
Lindgren, S. & Heiter, U. 2017, ArXiv e-prints
Majewski, S. R., Schiavon, R. P., Frinchaboy, P. M., et al. 2015, ArXiv e-prints
Mann, A. W., Brewer, J. M., Gaidos, E., Lépine, S., & Hilton, E. J. 2013a, Astronomische Nachrichten, 334, 18
Mann, A. W., Deacon, N. R., Gaidos, E., et al. 2014, AJ, 147, 160
Mann, A. W., Feiden, G. A., Gaidos, E., Boyajian, T., & von Braun, K. 2015, ApJ, 804, 64
Mann, A. W., Gaidos, E., & Ansdell, M. 2013b, ApJ
Mera, D., Chabrier, G., & Baraffe, I. 1996, ApJ, 459, L87+
Mészáros, S., Allende Prieto, C., Edvardsson, B., et al. 2012, AJ, 144, 120
Newton, E. R., Charbonneau, D., Irwin, J., et al. 2014, AJ, 147, 20
Newton, E. R., Charbonneau, D., Irwin, J., & Mann, A. W. 2015, ApJ, 800, 85
Nidever, D. L., Holtzman, J. A., Allende Prieto, C., et al. 2015, AJ, 150, 173
Passegger, V. M., Wende-von Berg, S., & Reiners, A. 2016, A&A, 587, A19
Rajpurohit, A. S., Reylé, C., Allard, F., et al. 2016, A&A, 596, A33
Rajpurohit, A. S., Reylé, C., Allard, F., et al. 2013, A&A, 556, A15
Rajpurohit, A. S., Reylé, C., Allard, F., et al. 2014, A&A, 564, A90
Rajpurohit, A. S., Reylé, C., Schultheis, M., et al. 2012, A&A, 545, A85
Reiners, A. 2005, Astronomische Nachrichten, 326, 930
Reiners, A., Mrotzek, N., Lemke, U., Hinrichs, J., & Reinsch, K. 2016, A&A, 587, A65
Renzini, A., Bragaglia, A., Ferraro, F. R., et al. 1996, ApJ, 465, L23+
Rojas-Ayala, B., Covey, K. R., Muirhead, P. S., & Lloyd, J. P. 2010, ApJ, 720, L113
Rojas-Ayala, B., Covey, K. R., Muirhead, P. S., & Lloyd, J. P. 2012, ApJ, 748, 93
Ruiz, J. 1997, Earth Moon and Planets, 77, 99
Schlaufman, K. C. & Laughlin, G. 2010, A&A, 519, A105
Schmidt, S. J., Wagoner, E. L., Johnson, J. A., et al. 2016, MNRAS, 460, 2611
Ségransan, D., Kervella, P., Forveille, T., & Queloz, D. 2003, A&A, 397, L5
Souto, D., Cunha, K., García-Hernández, D. A., et al. 2017, ApJ, 835, 239
Terrien, R. C., Mahadevan, S., Bender, C. F., et al. 2012, ApJ, 747, L38
Terrien, R. C., Mahadevan, S., Deshpande, R., & Bender, C. F. 2015, ApJS, 220, 16
Tsuji, T., Ohnaka, K., & Aoki, W. 1996a, A&A, 305, L1+
Tsuji, T., Ohnaka, K., Aoki, W., & Nakajima, T. 1996b, A&A, 308, L29
Valenti, J. A., Piskunov, N., & Johns-Krull, C. M. 1998, ApJ, 498, 851
Veeder, G. J. 1974, AJ, 79, 1056
Wilson, J. C., Hearty, F., Skrutskie, M. F., et al. 2010, in Proc. SPIE, Vol. 7735, Ground-based and Airborne Instrumentation for Astronomy III, 77351C
Wilson, J. C., Hearty, F., Skrutskie, M. F., et al. 2012, in Proc. SPIE, Vol. 8446, Ground-based and Airborne Instrumentation for Astronomy IV, 84460H
Wing, R. F. & Rinsland, C. P. 1979, AJ, 84, 1235
Woolf, V. M., Lépine, S., & Wallerstein, G. 2009, PASP, 121, 117
Woolf, V. M. & Wallerstein, G. 2006, PASP, 118, 218